

# Northumbria Research Link

Citation: Vo, Thuc, Guan, Zhongwei, Cantwell, Wesley and Schleyer, Graham (2013) Modelling of the low-impulse blast behaviour of fibre–metal laminates based on different aluminium alloys. *Composites Part B: Engineering* , 44 (1). 141 - 151. ISSN 1359-8368

Published by: Elsevier

URL: <http://dx.doi.org/10.1016/j.compositesb.2012.06.013>

This version was downloaded from Northumbria Research Link:  
<http://nrl.northumbria.ac.uk/13375/>

Northumbria University has developed Northumbria Research Link (NRL) to enable users to access the University's research output. Copyright © and moral rights for items on NRL are retained by the individual author(s) and/or other copyright owners. Single copies of full items can be reproduced, displayed or performed, and given to third parties in any format or medium for personal research or study, educational, or not-for-profit purposes without prior permission or charge, provided the authors, title and full bibliographic details are given, as well as a hyperlink and/or URL to the original metadata page. The content must not be changed in any way. Full items must not be sold commercially in any format or medium without formal permission of the copyright holder. The full policy is available online: <http://nrl.northumbria.ac.uk/policies.html>

This document may differ from the final, published version of the research and has been made available online in accordance with publisher policies. To read and/or cite from the published version of the research, please visit the publisher's website (a subscription may be required.)

[www.northumbria.ac.uk/nrl](http://www.northumbria.ac.uk/nrl)



1 Modelling of the low-impulse blast behaviour of fibre-metal laminates  
2  
3  
4 based on different aluminium alloys  
5  
6  
7

8 Thuc P. Vo\*, Z.W. Guan, W.J. Cantwell and G.K. Schleyer  
9

10 School of Engineering, University of Liverpool, Brownlow Street, Liverpool L69 3GQ, UK.  
11  
12  
13  
14  
15

16 **Abstract**  
17

18  
19 A parametric study has been undertaken in order to investigate the influence of the properties  
20  
21 of the aluminium alloy on the blast response of fibre-metal laminates (FMLs). The finite  
22  
23 element (FE) models have been developed and validated using experimental data from tests  
24  
25 on FMLs based on a 2024-O aluminium alloy and a woven glass-fibre/polypropylene  
26  
27 composite (GFPP). A vectorized user material subroutine (VUMAT) was employed to define  
28  
29 Hashin's 3D rate-dependant damage constitutive model of the GFPP. Using the validated  
30  
31 models, a parametric study has been carried out to investigate the blast resistance of FML  
32  
33 panels based on the four aluminium alloys, namely 2024-O, 2024-T3, 6061-T6 and 7075-T6.  
34  
35 It has been shown that there is an approximation linear relationship between the  
36  
37 dimensionless back face displacement and the dimensionless impulse for all aluminium alloys  
38  
39 investigated here. It has also shown that the residual displacement of back surface of the FML  
40  
41 panels and the internal debonding are dependent on the yield strength of the aluminium alloy.  
42  
43  
44  
45

46  
47 *Keywords:* A. Glass fibres; B. Mechanical properties; C. Damage mechanics; C. Numerical  
48  
49 analysis.  
50  
51

---

52  
53  
54  
55 \* Corresponding author, Tel.: +44 151 7945095; Fax: +44 151 7945218.

56  
57 Present address: School of Mechanical, Aeronautical and Electrical Engineering, Glyndwr University, Mold  
58  
59 Road, Wrexham LL11 2AW, UK.

60 E-mail address: [t.vo@glyndwr.ac.uk](mailto:t.vo@glyndwr.ac.uk)  
61  
62  
63  
64  
65

1 **1. Introduction**

2  
3  
4 Fibre-metal laminates (FMLs) are hybridised metal and composite structural materials that  
5  
6 have been attracting interest from a number of researchers due to their improved fatigue and  
7  
8 impact resistance ([1]-[6]). The most commonly used FML is GLARE, which comprises thin  
9  
10 aluminium 2024-T3 sheets and a unidirectional or a biaxial glass-fibre-reinforced epoxy. The  
11  
12 blast response of FMLs has received attention in a number of experimental studies. Fleischer  
13  
14 [7] presented data from blast test results on a lightweight luggage container based on GLARE  
15  
16 and reported that it was capable of withstanding a bomb blast greater than that in the  
17  
18 Lockerbie air disaster. Langdon et al. ([8]-[10]) carried out blast tests of FML panels based on  
19  
20 a 2024-O aluminium alloy and a glass fibre reinforced polypropylene. They observed a  
21  
22 number of failure mechanisms including multiple debonding, large plastic displacements,  
23  
24 fibre fracture and matrix cracking. Diamond, cross-shaped back face damage and front face  
25  
26 buckling were also observed. A dimensionless analysis showed that the front and back face  
27  
28 displacements fell within one plate thickness of a linear trend line. Blast tests on FML panels  
29  
30 based on other composites, such as a glass fibre polyamide matrix and GLARE were also  
31  
32 been undertaken by Langdon et al. ([11], [12]). Since experimental trials are usually very  
33  
34 costly and time-consuming, it is evident that modelling the blast behaviour of FMLs using  
35  
36 commercial finite element software would be great interest. Once these models are verified,  
37  
38 they can be used to predict the response of FMLs based on different configurations, lay-ups,  
39  
40 loading and boundary conditions without the need to undertake a large number of  
41  
42 experimental tests. However, in spite of the fact that there have been a number of  
43  
44 experimental studies on the blast behaviour of FMLs, relatively little work has been  
45  
46 conducted to model their response. Kotzakolios et al. [13] used LS-DYNA to investigate the  
47  
48 blast response of GLARE laminates-comparison against experimental results. This work also  
49  
50 included the numerical verification process for 50, 75, 100, 150 gram of explosive, and  
51  
52  
53  
54  
55  
56  
57  
58  
59  
60  
61  
62  
63  
64  
65

1 discusses the corresponding failure modes and strain rates. Later, Kotzakolios et al. [14]  
2 extended their research to investigate the damage induced in a typical commercial fuselage  
3 based on aluminium and GLARE, when subjected to an explosive charge. Simulations were  
4 performed for different charge locations in three stages: an initialization phase, a blast phase  
5 and a final phase. Soutis et al. [15] investigated the structural response of fully clamped  
6 GLARE panels to blast loads using LS-DYNA. Excellent agreement between the predicted  
7 and measured midpoint deflections and evidence of significant yield line deformation were  
8 highlighted. Karagiozova et al. [16] modelled the blast response of FML panels based on  
9 various stacking configurations using ABAQUS/Explicit in order to predict the influence of  
10 the loading parameters and structural characteristics on their overall behaviour. Although  
11 ABAQUS has a number of failure criteria for composite materials, they can only be used with  
12 2D elements, such as plane stress and continuum shell elements. Further, none of these  
13 criteria consider strain-rate effects in composite materials, which is clearly important in  
14 dynamic studies. The 2D elements, with the existing failure criteria, are not capable of taking  
15 large through-the-thickness rate-dependent deformations into account. Therefore, it is  
16 necessary to develop a constitutive model with associated failure criteria suitable for  
17 simulating a composite material using 3D solid elements. Recently, Vo et al. [17] developed  
18 FE models which were validated using experimental data from tests on FMLs based on a  
19 2024-O aluminium alloy and a woven glass-fibre/polypropylene composite. The rate-  
20 dependent failure criteria for a unidirectional composite were used, which were based on the  
21 modified Hashin's 3D failure criteria [18]. The constitutive model and failure criteria were  
22 then implemented in ABAQUS/Explicit using the VUMAT subroutine. Here, the analysis was  
23 restricted to low-impulse blast behaviour, which was defined according to Mode I failure from  
24 the experimental study carried out by Langdon et al. ([8]-[10]).

25 In this paper, based on the previous research [17], parametric studies were carried out to

1 investigate the influence of the properties of the aluminium alloy on the blast resistance of  
2 FMLs for aerospace applications. Here Johnson-Cook strain hardening and damage criterion  
3 were employed. Particular attention is given to predicting the front and back displacements  
4 and the energies dissipated during the blast process. In total, thirty-six cases are studied. It has  
5 been shown that there is an approximation linear relationship between the dimensionless back  
6 face displacement and the dimensionless impulse for all aluminium alloys investigated here. It  
7 has also shown that the residual displacement of back surface of the FML panels and the  
8 internal debonding are dependent on the yield strength of the aluminium alloy.  
9

## 20 **2. Geometric and Blast Loadings of FML Panels**

21 For verification purposes, the FML panels previously subjected to localised blast loading in  
22 the experimental study by Langdon et al. ([8]-[10]) are used to validate the current FE models.  
23 These 400×400 mm panels (300×300 mm exposed area), were manufactured from sheets of  
24 0.025 in. (approximately 0.6 mm) thick 2024-O aluminium alloy and a woven glass-  
25 fibre/polypropylene composite. The FML panels are identified using the notation, AXYZ-#,  
26 as described in [8], where A = aluminium, X = number of aluminium layers, T = GFPP, Y =  
27 number of blocks of GFPP, Z = number of plies of GFPP per block and # indicates the panel  
28 number. In order to promote better adhesion to the composite material, a thin layer of  
29 polypropylene (PP) film (Xiro 23.101) was placed between the chromate-coated aluminium  
30 alloy and the glass fibre reinforced PP composite. The panels were tested using a ballistic  
31 pendulum facility.  
32

33 In order to investigate the influence of the properties of the aluminium alloy on the low-  
34 impulse blast behavior, FML panels based on the four aluminium alloys, namely 2024-O,  
35 2024-T3, 6061-T6 and 7075-T6, subjected to an impulse  $I = 8$  Ns were considered. All four  
36 alloys are widely used in the aerospace industry. Details of the lay-ups and impulses  
37 investigated in this study are listed in Table 1.  
38  
39  
40  
41  
42  
43  
44  
45  
46  
47  
48  
49  
50  
51  
52  
53  
54  
55  
56  
57  
58  
59  
60  
61  
62  
63  
64  
65

1 The current research is concentrated on the cases where the explosive is placed on the surface  
 2 of the target. Therefore, converting the explosion to a surface impulsive pressure is likely to  
 3 be the most effective approach [16, 19, 20]. However, if the explosive is detonated at some  
 4 distance from the target, Arbitrary Lagrangian Eulerian (ALE) and CONWEP [21] should be  
 5 used to apply the blast load to the structure. Ideally, during an air-blast event, air and  
 6 detonation products, as well as the structural response of the target should be considered  
 7 simultaneously. Using the ALE approach, air and the detonation products may be described  
 8 using an Eulerian formulation in a gaseous domain, while the structural response can be  
 9 treated in a structural domain. A coupling algorithm for the fluid–structure interaction is then  
 10 employed to connect the two domains [14, 15]. However, this approach requires considerably  
 11 more computational time, especially for ABAQUS/Explicit. A blast analysis using the  
 12 pressure time history predicted by CONWEP or similar is likely save computational time and  
 13 is likely to produce a reasonably accurate response. For the reasons mentioned the above, the  
 14 blast load in this study is assumed to act impulsively and is applied using a pressure load  
 15 acting on the exposed face of the FML panel [16]. This pressure load, calculated from the  
 16 measured impulse, is a function of both time and distance from the plate centre. The pressure–  
 17 time history is idealized as a uniform function over a small central region and follows an  
 18 exponentially decaying function as:

$$P(r,t) = p_1(r)p_2(t) \quad (1)$$

46 where:

$$\begin{aligned}
 p_1(r) &= \begin{cases} P_0 & r \leq r_0 \\ P_0 e^{-k(r-r_0)} & r_0 < r < r_b \\ 0 & r > r_b \end{cases} \\
 p_2(t) &= e^{-2t/t_0}
 \end{aligned} \quad (2)$$

47 where  $r_0 = 15$  mm is the radius of the explosive disc used in the experiments,  $r_b < L/2$ ,  $L$  is  
 48 the length of the panel and  $t_0 = 0.008$  ms is the characteristic decay time for the pulse and  $k$  is

an exponential decay parameter. The decay parameter is not constant, but a function of the total impulse [16]. The total impulse is defined as:

$$I = 2\pi \int_0^{\infty} \int_0^r P(r,t) dr dt \quad (3)$$

A user subroutine VDLOAD was used to model the pressure distribution over the exposed area of the plate.

### 3. Material Modelling

#### 3.1 Aluminium layers

The aluminium alloy was modeled as an elasto-plastic material, exhibiting rate-dependent behaviour. Temperature effects in the aluminium alloy were not taken into account. The Johnson-Cook material model was used in the form:

$$\sigma = \left[ A + B(\bar{\varepsilon}_{pl})^n \right] \left[ 1 + C \ln \left( \frac{\dot{\varepsilon}_{pl}}{\dot{\varepsilon}_0} \right) \right] \quad (4)$$

where  $\bar{\varepsilon}_{pl}$  is the equivalent plastic strain;  $\dot{\varepsilon}_{pl}$  and  $\dot{\varepsilon}_0$  are the equivalent plastic and reference strain rate and  $A$ ,  $B$ ,  $C$  and  $n$  are material parameters.

Damage in the Johnson-Cook material model is predicted using the following cumulative damage law:

$$D = \sum \left( \frac{\Delta \bar{\varepsilon}_{pl}}{\bar{\varepsilon}_f^{pl}} \right) \quad (5)$$

in which:

$$\bar{\varepsilon}_f^{pl} = \left[ D_1 + D_2 \exp(D_3 \sigma^*) \right] \left[ 1 + D_4 \ln \left( \frac{\dot{\varepsilon}_{pl}}{\dot{\varepsilon}_0} \right) \right] \quad (6)$$

where  $\Delta \bar{\varepsilon}_{pl}$  is the increment of equivalent plastic strain during an increment in loading and

$\sigma^*$  is the mean stress normalised by the equivalent stress. The parameters  $D_1$ ,  $D_2$ ,  $D_3$ , and  $D_4$  are constants. Failure is assumed to occur when  $D = 1$ . Hence the current failure strain,  $\bar{\epsilon}_f^{pl}$ , and thus the accumulation of damage,  $D$ , is a function of the mean stress and the strain rate. The constants in the Johnson-Cook model for the four aluminium alloys used in this study are given in Table 2. The Young's modulus, Poisson's ratio and density of the various aluminium alloys were taken as  $E = 73.1$  GPa,  $\nu = 0.3$  and  $\rho = 2690$  kg/m<sup>3</sup>, respectively.

### 3.2 Glass fibre reinforced composite layers

#### 3.2.1 The 3D damage model for the composite material

Given that a woven glass-fibre/polypropylene composite layer is produced by placing fibres in a  $[0^0/90^0]$  pattern, the material behaviour within the plane of the laminate is similar in those two directions. There is therefore no need to separate the fibre and resin in order to simulate the overall response of the composite ply. Besides, the material tests carried out in this paper were based on the composite laminates, i.e. no individual tests to address fiber and resin separately. Therefore, Hashin's 3D failure criteria [18] are sufficient to simulate woven glass-fibre/polypropylene composite layer. The failure functions may be expressed as follows:

$$\begin{aligned}
 \text{Fibre tension } (\sigma_{11} \geq 0): F_f^t &= \left( \frac{\sigma_{11}}{X_{1t}} \right)^2 + \left( \frac{\sigma_{12}}{S_{12}} \right)^2 + \left( \frac{\sigma_{13}}{S_{13}} \right)^2, d_{ft} = 1 \\
 \text{Fibre compression } (\sigma_{11} < 0): F_f^c &= \frac{|\sigma_{11}|}{X_{1c}}, d_{fc} = 1 \\
 \text{Matrix tension } (\sigma_{22} + \sigma_{33} \geq 0): F_m^t &= \frac{(\sigma_{22} + \sigma_{33})^2}{X_{2t}^2} + \frac{\sigma_{23}^2 - \sigma_{22}\sigma_{33}}{S_{23}^2} + \frac{\sigma_{12}^2 + \sigma_{13}^2}{S_{12}^2}, d_{mt} = 1 \\
 \text{Matrix compression } (\sigma_{22} + \sigma_{33} < 0) & \\
 F_m^c &= \left[ \left( \frac{X_{2c}}{2S_{23}} \right)^2 - 1 \right] \frac{(\sigma_{22} + \sigma_{33})}{X_{2c}} + \frac{(\sigma_{22} + \sigma_{33})^2}{4S_{23}^2} + \frac{(\sigma_{23}^2 - \sigma_{22}\sigma_{33})}{S_{23}^2} + \frac{\sigma_{12}^2 + \sigma_{13}^2}{S_{12}^2}, d_{mc} = 1
 \end{aligned} \tag{7}$$

where  $X_{1t}$ ,  $X_{1c}$ ,  $X_{2t}$ ,  $X_{2c}$ ,  $S_{12}$ ,  $S_{13}$  and  $S_{23}$  are the various strength components [18] and  $d_{ft}$ ,  $d_{fc}$ ,  $d_{mt}$  and  $d_{mc}$  are the damage variables associated with the four failure modes.

The response of the material after damage initiation (which describes the rate of degradation



of the material stiffness once the initiation criterion is satisfied) is defined by the following equation:

$$\sigma = C(d) \cdot \varepsilon \quad (8)$$

where  $C(d)$  is a  $6 \times 6$  symmetric damaged matrix, whose non-zero terms can be written as:

$$\begin{aligned} C_{11} &= (1-d_f)E_1(1-\nu_{23}\nu_{32})\Gamma \\ C_{22} &= (1-d_f)(1-d_m)E_2(1-\nu_{13}\nu_{31})\Gamma \\ C_{33} &= (1-d_f)(1-d_m)E_3(1-\nu_{12}\nu_{21})\Gamma \\ C_{12} &= (1-d_f)(1-d_m)E_1(\nu_{21}+\nu_{31}\nu_{23})\Gamma \\ C_{23} &= (1-d_f)(1-d_m)E_2(\nu_{32}+\nu_{12}\nu_{31})\Gamma \\ C_{13} &= (1-d_f)(1-d_m)E_1(\nu_{31}+\nu_{21}\nu_{32})\Gamma \\ C_{44} &= (1-d_f)(1-s_{mt}d_{mt})(1-s_{mc}d_{mc})G_{12} \\ C_{55} &= (1-d_f)(1-s_{mt}d_{mt})(1-s_{mc}d_{mc})G_{23} \\ C_{66} &= (1-d_f)(1-s_{mt}d_{mt})(1-s_{mc}d_{mc})G_{13} \end{aligned} \quad (9)$$

where the global fibre and matrix damage variables as well as the constant  $\Gamma$  are also defined as:

$$\begin{aligned} d_f &= 1 - (1-d_{ft})(1-d_{fc}) \\ d_m &= 1 - (1-d_{mt})(1-d_{mc}) \\ \Gamma &= 1/(1-\nu_{12}\nu_{21}-\nu_{23}\nu_{32}-\nu_{13}\nu_{31}-2\nu_{21}\nu_{32}\nu_{13}) \end{aligned} \quad (10)$$

where  $E_i$  is the Young's modulus in the  $i$  direction,  $G_{ij}$  is the shear modulus in the  $i$ - $j$  plane and  $\nu_{ij}$  is the Poisson's ratio for transverse strain in the  $j$ -direction, when the stress is applied in the  $i$ -direction. The Young's moduli, shear's moduli, Poisson's ratios and strengths of the GFPP are given in Table 3.

The factors  $s_{mt}$  and  $s_{mc}$  in the definitions of the shear moduli are introduced to control the reduction in shear stiffness caused by tensile and compressive failure in the matrix respectively. The following values are recommended in ABAQUS [22]:  $s_{mt} = 0.9$  and  $s_{mc} = 0.5$ .

### 3.2.2 Strain-rate effects in the mechanical properties

The effects of strain-rate on the mechanical properties of a composite material are typically

1 modelled using strain-rate dependent functions for both the elastic modulus and the strength.  
 2  
 3 Yen [23] developed logarithmic functions to account for strain-rate effects in a composite  
 4  
 5 material as follows:  
 6

$$\begin{aligned}
 \{S_{RT}\} &= \{S_0\} \left( 1 + C_1 \ln \frac{\dot{\bar{\epsilon}}}{\dot{\epsilon}_0} \right) \\
 \{E_{RT}\} &= \{E_0\} \left( 1 + C_2 \ln \frac{\dot{\bar{\epsilon}}}{\dot{\epsilon}_0} \right)
 \end{aligned}
 \tag{11}$$

7  
 8  
 9  
 10  
 11  
 12  
 13  
 14  
 15 where:

$$\begin{aligned}
 \{\dot{\bar{\epsilon}}\} &= \{|\dot{\epsilon}_1| \quad |\dot{\epsilon}_2| \quad |\dot{\epsilon}_1| \quad |\dot{\epsilon}_2| \quad |\dot{\epsilon}_{12}| \quad |\dot{\epsilon}_{13}| \quad |\dot{\epsilon}_{23}|\}^T \\
 \{S_{RT}\} &= \{X_{1t} \quad X_{2t} \quad X_{1c} \quad X_{2c} \quad S_{12} \quad S_{13} \quad S_{23}\}^T \\
 \{E_{RT}\} &= \{E_1 \quad E_2 \quad E_3 \quad G_{12} \quad G_{13} \quad G_{23}\}^T
 \end{aligned}
 \tag{12}$$

16  
 17  
 18  
 19  
 20  
 21  
 22  
 23  
 24 and the subscript ‘RT’ refers to the rate-adjusted values, the subscript ‘0’ refers to the static  
 25  
 26 value,  $\dot{\epsilon}_0 = 1 \text{ s}^{-1}$  is the reference strain-rate,  $\dot{\bar{\epsilon}}$  is the effective strain-rate,  $C_1$  and  $C_2$  are the  
 27  
 28 strain-rate constants, respectively.  
 29  
 30  
 31  
 32

### 33 *3.2.3 Implementation of the material model in ABAQUS/Explicit*

34  
 35  
 36 The material model and failure criteria described in the previous sections were implemented  
 37  
 38 in ABAQUS/Explicit using the VUMAT subroutine. This subroutine is compiled and enables  
 39  
 40 ABAQUS/Explicit to obtain the required information regarding the state of the material and  
 41  
 42 the material mechanical response during each time step, at each integration point of each  
 43  
 44 element. The stresses are computed within the VUMAT subroutine using the given strains and  
 45  
 46 the material stiffness coefficients. Based on these stresses, Hashin's 3D failure criteria  
 47  
 48 outlined in Eq.(7) are calculated, and the elastic modulus and strength values are adjusted for  
 49  
 50 strain-rate effects using Eq.(11). When an element fails, as determined by the failure criteria,  
 51  
 52 the element status is then changed from 1 to 0. At this point, the stresses at that material point  
 53  
 54 are reduced to zero and it no longer contributes to the model stiffness. When all of the  
 55  
 56  
 57  
 58  
 59  
 60  
 61  
 62  
 63  
 64  
 65

1 material status points of an element have been reduced to zero, the element is removed from  
2 the mesh.  
3

### 4 5 6 *3.3 Cohesive elements and material properties*

7  
8 Debonding at the interface between the composite and aluminium layers was modelled using  
9 cohesive elements available in ABAQUS [22]. The elastic response was defined in terms of a  
10 traction-separation law with uncoupled behaviour between the normal and shear components.  
11 The default choice of the constitutive thickness for modeling the response, in terms of traction  
12 versus separation, is 1.0, regardless of the actual thickness of the cohesive layer. Thus, the  
13 diagonal terms in the elasticity matrix and density should be calculated using the true  
14 thickness of the cohesive layer as follows:  
15  
16  
17  
18  
19  
20  
21  
22  
23  
24

$$25 \quad K_{nn} = \frac{E_n}{t_c}; \quad K_{ss} = \frac{E_s}{t_c}; \quad K_{tt} = \frac{E_t}{t_c} \quad (13)$$
$$26 \quad \rho = \rho_c t_c$$

27  
28  
29  
30

31 The quadratic nominal stress and energy criterion were used to model damage initiation and  
32 damage evolution, respectively. Damage initiated when a quadratic interaction function,  
33 involving the nominal stress ratios, reached unity. Damage evolution was defined based on the  
34 energy conjunction with a linear softening law. The mechanical properties of the cohesive  
35 elements were obtained from Karagiozova et al. [16] and are given in Table 4.  
36  
37  
38  
39  
40  
41  
42  
43

## 44 **4. Finite Element Modelling**

45  
46  
47 The 3D FML panel consisted of the aluminium alloy, the composite and the cohesive layers as  
48 three separate parts. The aluminium and composite layers were meshed using C3D8R  
49 elements, which are eight-noded, linear hexahedral elements with reduced integration and  
50 hourglass control. The interfaces between the aluminium and the composite layers were  
51 created using eight-node 3D cohesive elements (COH3D8). As the structure has symmetry in  
52 both the directions, only a quarter of each FML panel was modeled with the appropriate  
53  
54  
55  
56  
57  
58  
59  
60  
61  
62  
63  
64  
65

1 boundary conditions applied along the planes of symmetry, as shown in Figure 1. A mesh size  
2 of  $1 \times 1$  mm for a central area of  $60 \times 60$  mm (Figure 1) was found to be the most appropriate  
3 for these FML panels. Symmetric boundary conditions were applied to the nodes lying on the  
4 XY and YZ planes, while the other two edges were fully fixed. The general contact algorithm  
5 was used for the definition of contact between the two neighbouring layers of the aluminum  
6 and the composite. Detailed finite element modelling can be found in the paper by Vo, et al.  
7 [17].  
8  
9  
10  
11  
12  
13  
14  
15  
16  
17

## 18 **5. Results and Discussion**

21 Since there are no experimental data available in the literature to describe strain-rate effects in  
22 the woven glass-fibre/polypropylene composite, rate-dependent material models, with  
23 different values of the strain-rate constant, were investigated in this study. A material model  
24 incorporating strain-rate effects in the strength, shear and the through-thickness modulus  
25 values was chosen. Strain-rate constant values that agreed well with the experimental results  
26 were  $C_1 = C_2 = 0.35$ . This material model is consistent with results of McCarthy et al. [24] and  
27 Gama and Gillespie [25]. In their research, strain-rate effects were not taken into account for  
28 the in-plane elastic moduli  $E_1$  and  $E_2$  of the composite layers. Initially, two FML panels,  
29 A3T24-8 and A4T34-5, were studied to investigate their transient and residual displacements.  
30 After conducting a number of convergence studies, numerical simulations were carried out  
31 over a time period of 4 ms. The transient displacement relates to the first peak in the  
32 displacement time trace and the residual displacement is taken as the average after more than  
33 three cycles following unloading. The variation of the front and back displacements with time  
34 are shown in Figure 2. Here, the highly dynamic response of the panels is clearly evident with  
35 the displacements oscillating significantly in response to the blast event. As expected, the  
36 deflections of the thinner A3T24 panel are greater than those of its stiffer A4T34 counterpart.  
37 It is worth noting that the difference between the front and back surface displacements is  
38  
39  
40  
41  
42  
43  
44  
45  
46  
47  
48  
49  
50  
51  
52  
53  
54  
55  
56  
57  
58  
59  
60  
61  
62  
63  
64  
65

1 greater than the initial thickness of the panel. This increase in the effective thickness of the  
2 FML is associated with the opening up of planes of delamination within the volume of the  
3 laminate. Due to the relatively low impulse, there is a large elastic oscillation regime in the  
4 dynamic response of these panels. FE models of other types of FML panels subjected to a low  
5 impulse were also developed to broaden the validation. The experimental and numerical  
6 results are presented in Table 5. Reasonable agreement between the predicted and  
7 experimental mid-point displacements is observed. Closer examination of data suggests that  
8 the model tends to under-estimate the front surface displacement and over-estimate the back  
9 surface deformation of the targets. There are large differences between the back face and the  
10 front face displacements, which indicate the interfacial failure. Comparing the experimental  
11 and numerical failure modes of five typical panels, as shown in Figure 3, the simulations  
12 accurately capture the primary failure mechanisms in the FMLs, which include large out-of-  
13 plane plastic displacements, debonding of the back face and local buckling of the internal  
14 aluminium layer.

15  
16  
17  
18  
19  
20  
21  
22  
23  
24  
25  
26  
27  
28  
29  
30  
31  
32  
33  
34 The numerical results corresponding to FML panels based on the four aluminium alloys are  
35 presented in Table 6. It can be seen that the front and back displacements of those panels  
36 based on the aluminium 7075-T6 are the smallest, whereas those based on the aluminium  
37 2024-O are the largest. This suggests that the properties of the aluminium alloy, most  
38 particularly its yield stress, greatly influence the blast response of these hybrid materials. The  
39 4/3 A4T32-4 panel was chosen to investigate the transient response, deformed shapes and  
40 energy histories of four types of panel. Figure 4 shows comparisons of the variation of the  
41 front and back displacements with time. The deformed shapes of the A4T32-4 panel based on  
42 the four aluminium alloys are shown in Figure 5. It can be seen that the permanent  
43 displacements tend to decrease with increasing yield strength of the aluminium alloy, as  
44 shown in Figure 6. In this case, the permanent displacement of the A4T32 panel based on the  
45 2024-O alloy is almost double that of the aluminium 7075-T6. Figure 7 shows the variation of  
46  
47  
48  
49  
50  
51  
52  
53  
54  
55  
56  
57  
58  
59  
60  
61  
62  
63  
64  
65

1 the energy dissipated in debonding with the yield strength of the aluminium alloy. From the  
 2 figure, it is evident that this energy increases with the properties of the alloy, supporting the  
 3 observations in Figure 5 which suggest that the debonding area also increases with  $\sigma_y$ . Since  
 4 there is no splitting damage in the composite material, and assuming that the energy  
 5 associated with delaminating the composite layers is negligible, the energy balance using the  
 6 total energy quantities computed by ABAQUS is given by:

$$14 \quad E_{TOTAL} = IE_{ALL} + KE_{ALL} - WK_{ALL} = \text{constant} \quad (14)$$

17 where  $KE_{ALL}$  is the kinetic energy,  $WK_{ALL}$  is the external work and  $IE_{ALL}$  is the total internal  
 18 energy, defined by:

$$24 \quad IE_{ALL} = SE_{ALL} + PD_{ALL} + ED_{ALL} + AE_{ALL} \quad (15)$$

27 where  $SE_{ALL}$  is the recoverable strain energy,  $PD_{ALL}$  is the plastic dissipation energy,  $ED_{ALL}$  is  
 28 the energy dissipated by debonding and  $AE_{ALL}$  is the artificial strain energy.

31 The time histories of the kinetic ( $KE_{ALL}$ ) and the total internal energies ( $IE_{ALL}$ ) for the four  
 32 cases were determined and are shown in Figure 8. As  $E_{TOTAL}$  remains constant, the energy  
 33 balance is clearly maintained throughout the analysis. The kinetic energy ( $KE_{ALL}$ ) increases  
 34 and reaches a maximum value at an early stage of the blast event, and then, decreases. In  
 35 contrast, the internal energy ( $IE_{ALL}$ ) increases from zero and exhibits small oscillations, before  
 36 reaching a maximum value. The external work ( $WK_{ALL}$ ) and the components of the total  
 37 internal energy ( $IE_{ALL}$ ) are presented in Figure 9. Here, the ‘artificial energy’ ( $AE_{ALL}$ ) is the  
 38 energy associated with the application of hourglass control in ABAQUS, which prevents  
 39 excessive distortion of the mesh. It can be seen that the ‘artificial energy’ ( $AE_{ALL}$ ) is  
 40 significantly lower than the internal energy ( $IE_{ALL}$ ), indicating that the solution is trustworthy  
 41 ([22]). Figure 9 also indicates that most of the work done by the blast load is dissipated in  
 42 plastic deformation of the aluminium alloy and debonding of the composite and metal layers.  
 43  
 44  
 45  
 46  
 47  
 48  
 49  
 50  
 51  
 52  
 53  
 54  
 55  
 56  
 57  
 58  
 59  
 60  
 61  
 62  
 63  
 64  
 65

1 Debonding of the cohesive layer absorbs a small proportion of the blast energy, relative to the  
2 energy dissipated in plastically deforming the aluminium. It can be seen that for a given  
3 impulse, the FML based on the 2024-O alloy absorbs the greatest amount of energy in plastic  
4 deformation. It is worth noting, however, that the energy dissipated in plastic deformation of  
5 the alloy decreases as its yield strength increases. Here, this additional available energy is  
6 absorbed in debonding the composite and metal layers, as previously observed in Figure 7.  
7 This suggests that introducing an alloy with a higher yield strength allows for greater out-of-  
8 plane elastic deformations during the blast event (the yield strain will be higher). As these  
9 elastic displacements increase, the interfaces between the composite and metal layers are  
10 likely to fracture, leading to debonding between the constituent materials. This may explain  
11 why the levels of debonding are greater in the higher strength alloys.

12 In an attempt to compare FML panels based on different aluminium alloys, the most  
13 appropriate way to do this is by employing the dimensionless analysis used by Langdon et al.  
14 ([9], [26]). Here, the dimensionless impulse and displacements are given by:

$$\begin{aligned}
\Phi_q &= \frac{I(1 + \ln \frac{BL}{\pi r_0^2})}{2t^2 \sqrt{BL\rho\sigma_{UTS}}} \\
\delta_B &= \frac{d_B}{t}
\end{aligned} \tag{16}$$

15 where  $\rho$  is the material density,  $B$ ,  $L$  are the plate width and length dimensions,  $t$  is the plate  
16 thickness and  $\sigma_{UTS}$ : effective ultimate tensile strength. Reyes and Cantwell [6] showed that  
17 the tensile strength of FMLs can be approximated using the rule of mixtures by using:

$$\sigma_{UTS} = \frac{(\sigma_{UTS_{Al}} t_{Al} + \sigma_{UTS_{com}} t_{com})}{t} \tag{17}$$

18 Using the constituent properties of the aluminium alloy in Table 2, the effective ultimate  
19 tensile strength values were calculated and are given in Table 7.

1 The dimensionless back displacements of the FML panels are given in Table 6 and plotted  
2 against the dimensionless impulse in Figure 10. As expected, there is a reasonably linear  
3 relationship between the dimensionless back displacement and the dimensionless impulse for  
4 the FMLs based on the four types of aluminium alloy. Clearly, there is some scatter in the data,  
5 which is due to the difference in stacking sequences and thicknesses between the different  
6 FMLs, especially for A5T42 that consists of five aluminium layers and four composite layers.  
7 The equation for dimensionless impulse assumes that the yield stress obeys a rule of mixtures  
8 approach. This applies in tension but is less accurate in bending. Changing the thickness and  
9 the stacking sequence will lead to errors associated with the limitations related to this rule of  
10 mixtures approach. In addition, Eq. (17) applies to the in-plane properties of the FMLs, rather  
11 than their flexural behaviour. Figure 10 highlights the influence of the properties of the  
12 aluminium alloy on the blast resistance of FMLs. The trend-lines are almost parallel to each  
13 other, with the uppermost line corresponding to the FML based on the 2024-O alloy and the  
14 lowest to the 7075-T6 FML. The trend-line equations for the back face dimensionless  
15 displacements are given by:

$$\begin{aligned}
36 \quad & \text{Aluminium 2024-O: } \delta_B = 0.80\Phi_q + 0.87, R^2 = 0.90 \\
37 \quad & \text{Aluminium 2024-T3: } \delta_B = 0.76\Phi_q + 0.52, R^2 = 0.93 \\
38 \quad & \text{Aluminium 6061-T6: } \delta_B = 0.79\Phi_q + 0.63, R^2 = 0.94 \\
39 \quad & \text{Aluminium 7075-T6: } \delta_B = 0.64\Phi_q + 0.35, R^2 = 0.82
\end{aligned} \tag{18}$$

## 45 6. Conclusions

46 A parametric study of the low-impulse blast behaviour of FMLs based on different aluminium  
47 alloys is presented. Here, three dimensional finite element models of FML panels based on a  
48 2024-O aluminium alloy and a woven glass-fibre/polypropylene composite subjected to low-  
49 impulse localised blast loading are developed and validated against previously-published  
50  
51  
52  
53  
54  
55  
56  
57  
58  
59  
60  
61  
62  
63  
64  
65



1 experimental data. Hashin's 3D failure criteria, incorporating strain-rate effects in the GFPP is  
2  
3  
4 implemented into ABAQUS/Explicit. Using the validated models, a parametric study is used  
5  
6  
7 to investigate the influence of the properties of the aluminium alloy on the blast resistance of  
8  
9  
10 FMLs based on the four aluminium alloys, namely 2024-O, 2024-T3, 6061-T6 and 7075-T6.  
11  
12  
13 The residual back displacement of the FML panels decreases with the increasing yield  
14  
15  
16 strength of the aluminium alloy. Using a dimensionless analysis procedure, it has been shown  
17  
18  
19 that there is an approximate linear relationship between the dimensionless back surface  
20  
21  
22 displacement and the dimensionless impulse for all aluminium alloys investigated here.  
23  
24  
25  
26 However, changing the thickness and the stacking sequence is likely lead to errors associated  
27  
28  
29 with the limitations related to this rule of mixtures approach. It has also been shown that the  
30  
31  
32 level of debonding is strongly dependent on the yield characteristics of the aluminium alloy.  
33  
34  
35  
36 Given that the aluminium alloy does not rupture in these analyses, the failure strain is not  
37  
38  
39 influencing the response of the panels. The elastic moduli of the alloys are all similar so that  
40  
41  
42 this is not considered to be an important parameter in this investigation. The evidence  
43  
44  
45 suggests that the 7075-T6 alloy offers the best resistance to blast loading of the laminates  
46  
47  
48 considered.

## 51 **7. Acknowledgments**

52  
53  
54  
55  
56 The authors would like to thank the Leverhulme Trust for the financially supporting the work  
57  
58 presented in this paper. The authors also would like to acknowledge the use of the UK  
59  
60  
61  
62  
63  
64  
65

1 National Grid Service in carrying out this work.  
2  
3

## 4 **8. References**

5  
6  
7 [1] A. Vlot, Impact loading on fibre metal laminates, *International Journal of Impact*  
8 *Engineering* 18 (3) (1996) 291 – 307.  
9

10  
11  
12 [2] S. Krishnakumar, Fibre metal laminates-the synthesis of metals and composites,  
13 *Materials and Manufacturing Processes* 9 (2) (1994) 295–354.  
14  
15

16  
17  
18 [3] L. B. Vogelesang, A. Vlot, Development of fibre metal laminates for advanced  
19 *aerospace structures*, *Journal of Materials Processing Technology* 103 (1) (2000) 1 – 5.  
20  
21

22  
23  
24 [4] P. Compston, W. J. Cantwell, C. Jones, N. Jones, Impact perforation resistance and  
25 *fracture mechanisms of a thermoplastic based fiber-metal laminate*, *Journal of Materials*  
26 *Science Letters* 20 (2001) 597–599.  
27  
28

29  
30  
31 [5] G. Reyes-Villanueva, W. J. Cantwell, The high velocity impact response of composite  
32 *and FML-reinforced sandwich structures*, *Composites Science and Technology* 64 (1) (2004)  
33 35 – 54.  
34  
35

36  
37  
38 [6] G. Reyes, W. J. Cantwell, The mechanical properties of fibre-metal laminates based on  
39 *glass fibre reinforced polypropylene*, *Composites Science and Technology* 60 (7) (2000) 1085  
40 – 1094.  
41  
42

43  
44  
45 [7] H. J. Fleisher, Design and explosive testing of a blast resistant luggage container, in:  
46 *International conference on structures under shock and impact*, 1996, pp. 51–60.  
47  
48

49  
50  
51 [8] G. S. Langdon, S. L. Lemanski, G. N. Nurick, M. C. Simmons, W. J. Cantwell, G. K.  
52 *Schleyer*, Behaviour of fibre-metal laminates subjected to localised blast loading: Part I–  
53  
54

1 Experimental observations, *International Journal of Impact Engineering* 34 (7) (2007) 1202 –  
2  
3 1222.

4  
5  
6 [9] S. L. Lemanski, G. N. Nurick, G. S. Langdon, M. C. Simmons, W. J. Cantwell, G. K.  
7  
8 Schleyer, Behaviour of fibre metal laminates subjected to localised blast loading–Part II:  
9  
10 Quantitative analysis, *International Journal of Impact Engineering* 34 (7) (2007) 1223 – 1245.

11  
12  
13 [10] G. S. Langdon, G. N. Nurick, S. L. Lemanski, M. C. Simmons, W. J. Cantwell, G. K.  
14  
15 Schleyer, Failure characterisation of blast-loaded fibre-metal laminate panels based on  
16  
17 aluminium and glass-fibre reinforced polypropylene, *Composites Science and Technology*  
18  
19 67 (7-8) (2007) 1385 – 1405.

20  
21  
22 [11] G. S. Langdon, W. J. Cantwell, G. N. Nurick, Localised blast loading of fibre-metal  
23  
24 laminates with a polyamide matrix, *Composites Part B: Engineering* 38 (7-8) (2007) 902 –  
25  
26 913.

27  
28  
29 [12] G. S. Langdon, Y. Chi, G. N. Nurick, P. Haupt, Response of GLARE© panels to blast  
30  
31 loading, *Engineering Structures* 31 (12) (2009) 3116 – 3120.

32  
33  
34 [13] T. Kotzakolios, D. Vlachos, V. Kostopoulos, Investigation of blast response of GLARE  
35  
36 laminates: comparison against experimental results, *Plastics, Rubber and Composites* 40 (6-7)  
37  
38 (2011) 349 – 355.

39  
40  
41 [14] T. Kotzakolios, D. Vlachos, V. Kostopoulos, Blast response of metal composite laminate  
42  
43 fuselage structures using finite element modelling, *Composite Structures* 93 (2) (2011) 665 –  
44  
45 681.

46  
47  
48 [15] C. Soutis, G. Mohamed, A. Hodzic, Modelling the structural response of glare panels to  
49  
50 blast load, *Composite Structures* 94 (1) (2011) 267 – 276.

- 1 [16] D. Karagiozova, G. S. Langdon, G. N. Nurick, S. C. K. Yuen, Simulation of the  
2 response of fibre-metal laminates to localised blast loading, *International Journal of Impact*  
3 *Engineering* 37 (6) (2010) 766 – 782.  
4  
5  
6  
7  
8 [17] T.P. Vo, Z. W. Guan, W. J. Cantwell and G. K. Schleyer, Low-impulse blast behaviour of  
9 fibre-metal laminates, *Composite Structures* 94 (3) (2012) 954-965.[18]  
10  
11  
12  
13 [18] Z. Hashin, Failure criteria for unidirectional fiber composites, *Journal of Applied*  
14 *Mechanics* 47 (1980) 329–334.  
15  
16  
17  
18  
19 [19] G. S. Langdon, Yuen, S. C. K. Yuen and G. N. Nurick, Experimental and numerical  
20 studies on the response of quadrangular stiffened plates. Part II: localised blast loading,  
21 *International Journal of Impact Engineering* 31(1) (2005) 85 - 111  
22  
23  
24  
25  
26  
27 [20] D. Karagiozova, G. N. Nurick and G. S. Langdon, Behaviour of sandwich panels subject  
28 to intense air blasts - Part 2: Numerical simulation, *Composite Structures*, 2009, 91 (4), 442 –  
29 450  
30  
31  
32  
33  
34  
35 [21] C. N. Kingery, G. Bulmash and U. A. B. R. Laboratory, Air blast parameters from TNT  
36 spherical air burst and hemispherical surface burst, *Ballistic Research Laboratories*, 1984.  
37  
38  
39  
40  
41 [22] ABAQUS, Theory Manual, Version 6.9, Hibbitt, Karlsson & Sorensen, Inc. (2009).  
42  
43  
44 [23] C. F. Yen, Ballistic impact modeling of composite materials, in: *Proceedings of the 7th*  
45 *International LS-DYNA Users Conference*, Vol. 6, 2002, pp. 15–23.  
46  
47  
48  
49  
50 [24] M. A. McCarthy, J. R. Xiao, N. Petrinic, A. Kamoulakos, V. Melito, Modelling of bird  
51 strike on an aircraft wing leading edge made from fibre metal laminates- part 1: Material  
52 modelling, *Applied Composite Materials* 11 (2004) 295–315.  
53  
54  
55  
56  
57  
58  
59  
60  
61  
62  
63  
64  
65

1 [25] B. A. Gama, J. W. Gillespie Jr., Finite element modeling of impact, damage evolution  
2 and penetration of thick-section composites, International Journal of Impact Engineering  
3 38 (4) (2011) 181 – 197.  
4  
5  
6

7  
8 [26] G. S. Langdon, W. J. Cantwell, G. N. Nurick, The blast response of novel thermoplastic-  
9 based fibre-metal laminates - some preliminary results and observations, Composites Science  
10 and Technology 65 (6) (2005) 861 – 872.  
11  
12  
13  
14  
15

16 [27] D. R. Lesuer, Experimental Investigations of Material Models for Ti-6Al-4V Titanium  
17 and 2024-T3 Aluminum, Tech. rep., Lawrence Livermore National Laboratory, Livermore,  
18 CA. (2000).  
19  
20  
21  
22  
23

24 [28] B. Corbett, Numerical simulations of target hole diameters for hypervelocity impacts  
25 into elevated and room temperature bumpers, International Journal of Impact Engineering  
26 33 (1-12) (2006) 431 – 440.  
27  
28  
29  
30  
31

32 [29] N. S. Brar, V. S. Joshi, B. W. Harris, Constitutive model constants for Al7075-T651 and  
33 Al7075-T6, AIP Conference Proceedings 1195 (1) (2009) 945–948.  
34  
35  
36  
37  
38  
39  
40  
41  
42  
43  
44  
45  
46  
47  
48  
49  
50  
51  
52  
53  
54  
55  
56  
57  
58  
59  
60  
61  
62  
63  
64  
65

## CAPTIONS OF FIGURES

1  
2  
3  
4 Figure 1: Dimensions, loading, boundary conditions and mesh generation for typical 3/2 FML  
5  
6 panel.

7  
8 Figure 2: Back and front face displacements versus time for panels A3T24-8 and A4T34-5.

9  
10  
11 Figure 3: Comparison between the experiments and numerical simulations for five FML panel  
12  
13 s.

14  
15 Figure 4: Back and front face displacements versus time for the A4T32-  
16  
17 4 panel based on the four aluminium alloys.

18  
19  
20 Figure 5: Deformed shapes of the A4T32-4 panel based on the four aluminium alloys.

21  
22 Figure 6: Residual front and back face displacements of the A4T32-  
23  
24 4 panel based on the four aluminium alloys versus yield strength.

25  
26  
27 Figure 7: Debonding energy of the A4T32-  
28  
29 4 panel based on the four aluminium alloys versus yield strength.

30  
31  
32 Figure 8: The time history of total internal energy and kinetic energy of the A4T32-  
33  
34 4 panel based on the four aluminium alloys.

35  
36  
37 Figure 9: External work and total internal energy components (PD, SE, ED and AE) of the A  
38  
39 4T32-4 panel based on the four aluminium alloys.

40  
41  
42 Figure 10: Graph of dimensionless permanent displacement of back face versus dimensionless  
43  
44 impulse.

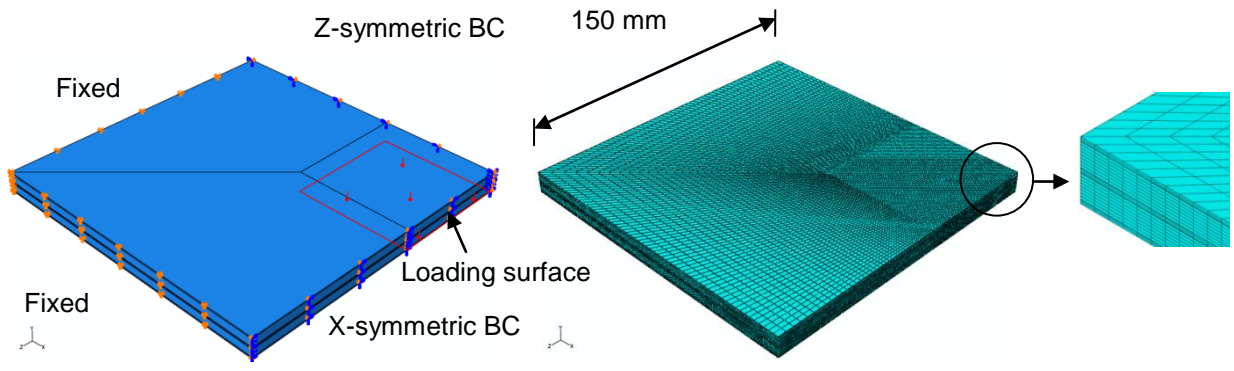


Figure 1: Dimensions, loading, boundary conditions and mesh generation for typical 3/2 FML panel.

1  
2  
3  
4  
5  
6  
7  
8  
9  
10  
11  
12  
13  
14  
15  
16  
17  
18  
19  
20  
21  
22  
23  
24  
25  
26  
27  
28  
29  
30  
31  
32  
33  
34  
35  
36  
37  
38  
39  
40  
41  
42  
43  
44  
45  
46  
47  
48  
49  
50  
51  
52  
53  
54  
55  
56  
57  
58  
59  
60  
61  
62  
63  
64  
65

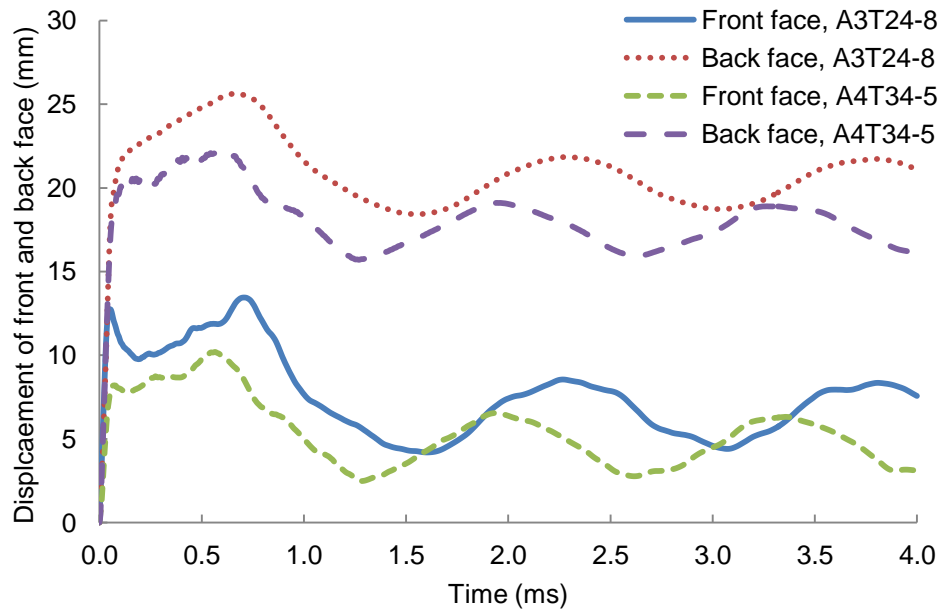
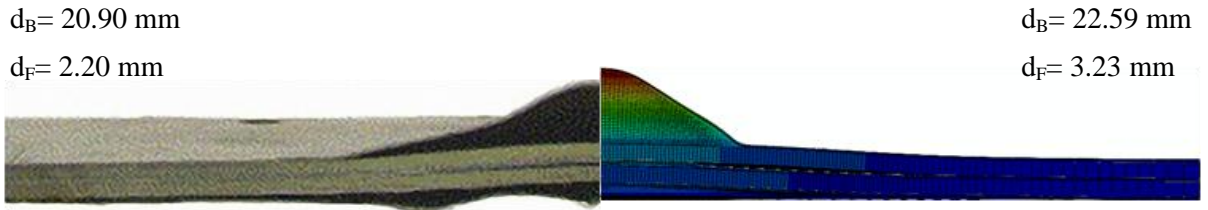
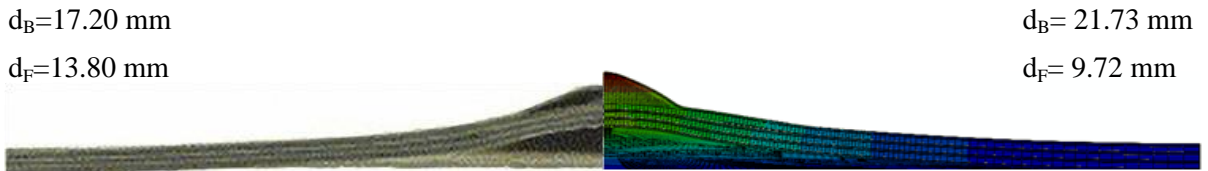


Figure 2: Back and front face displacements versus time for panels A3T24-8 and A4T34-5.

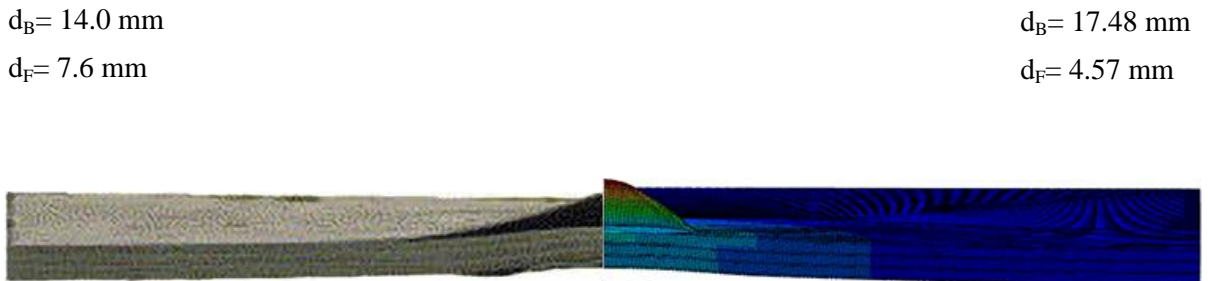




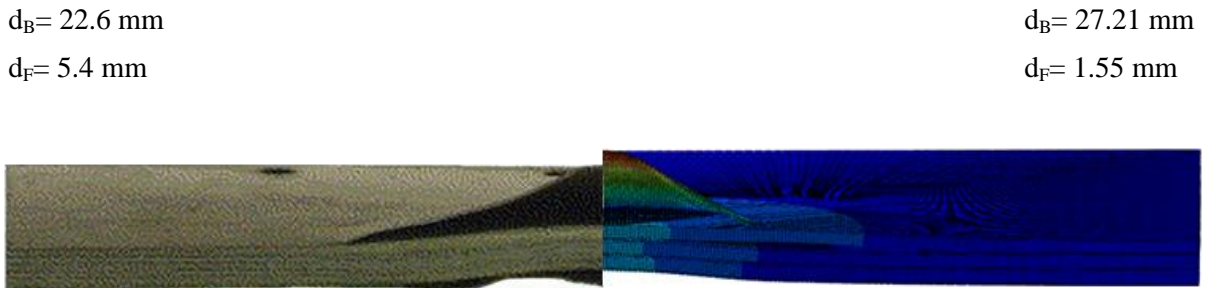
9 a. A3T28-5,  $I = 10.34$  Ns



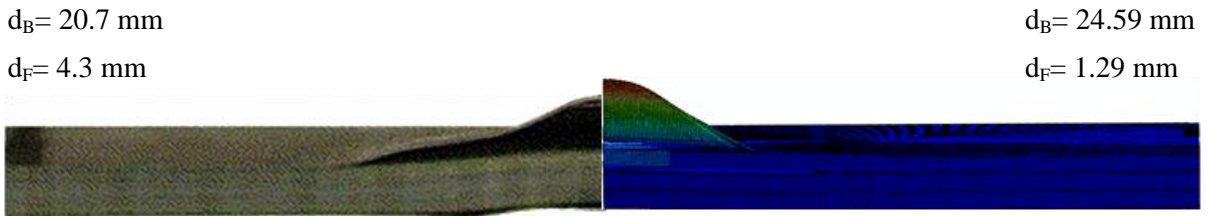
18 b. A4T32-4,  $I = 7.23$  Ns



30 c. A4T34-5,  $I = 7.01$  Ns

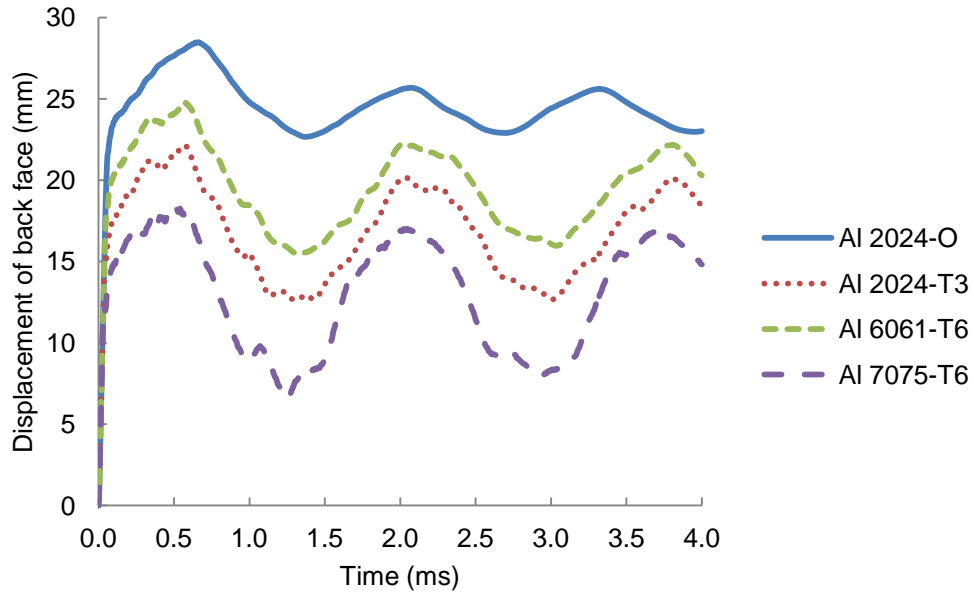


43 d. A4T36-2,  $I = 11.61$  Ns

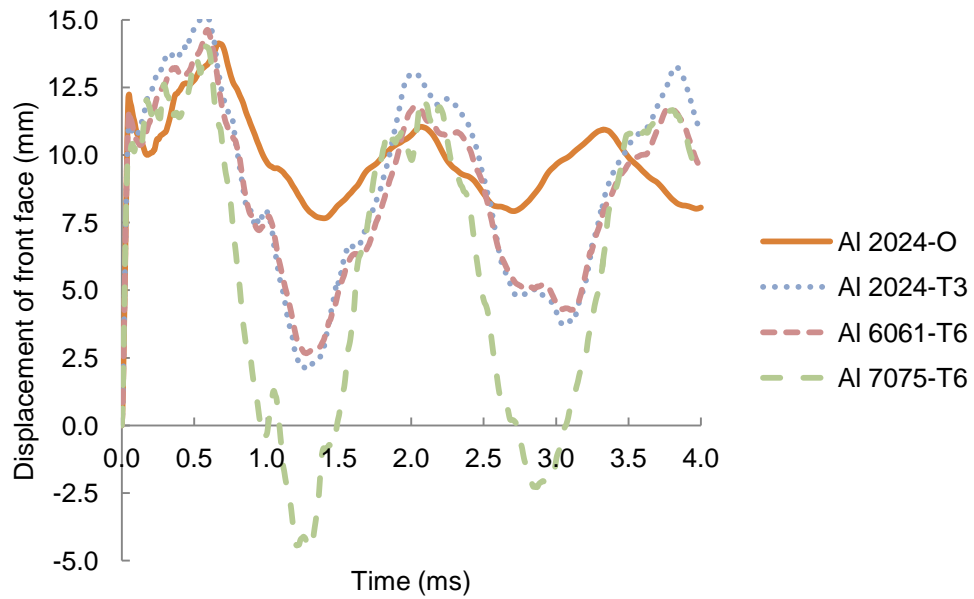


54 e. A4T38-2,  $I = 11.13$  Ns

55  
 56  
 57 Figure 3: Comparison between the experiments and numerical simulations for five FML  
 58 panels.  
 59  
 60  
 61

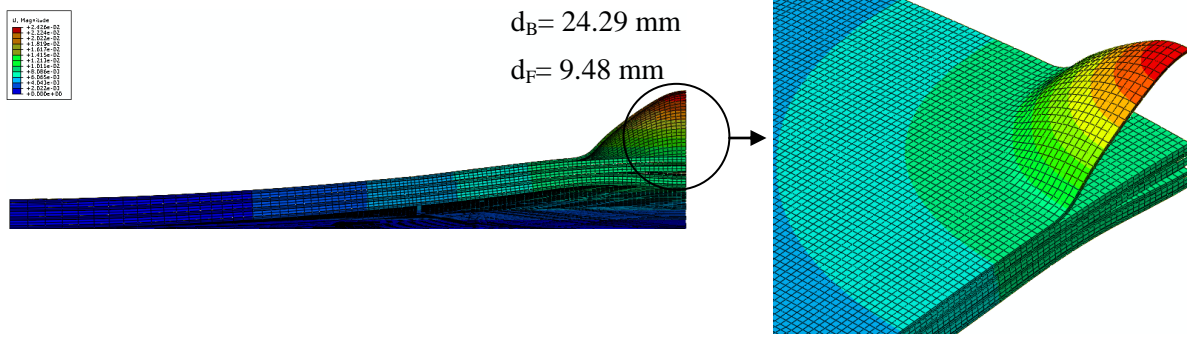


a. Back displacement

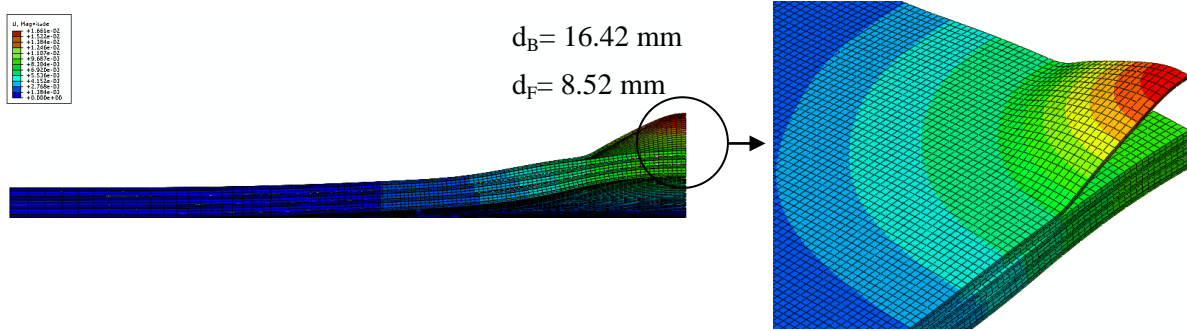


b. Front displacement

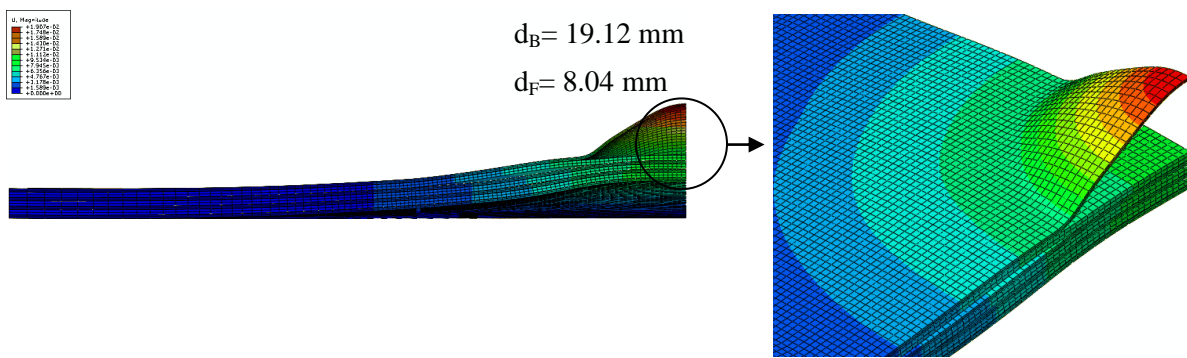
Figure 4: Back and front face displacements versus time for the A4T32-4 panel based on the four aluminium alloys.



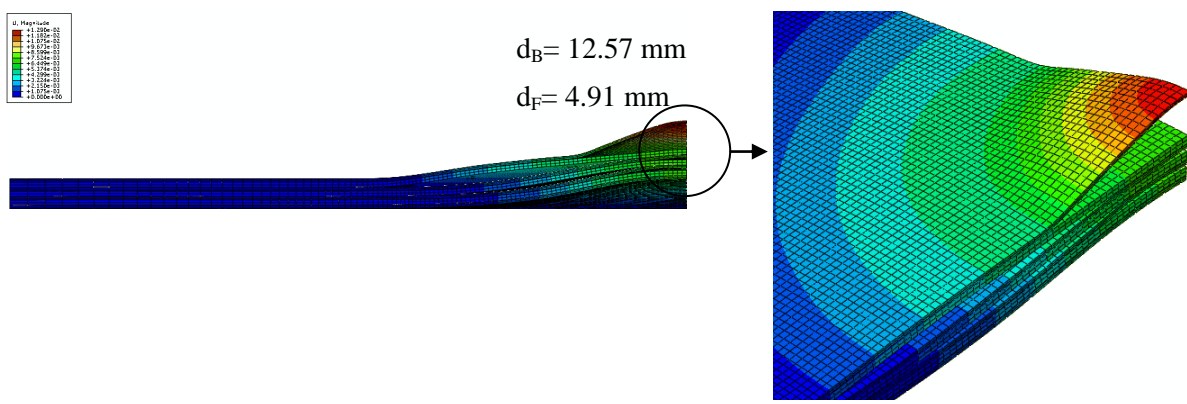
a. Al 2024-O



b. Al 2024-T3



c. Al 6061-T6



d. Al 7075-T6

Figure 5: Deformed shapes of the A4T32-4 panel based on the four aluminium alloys.

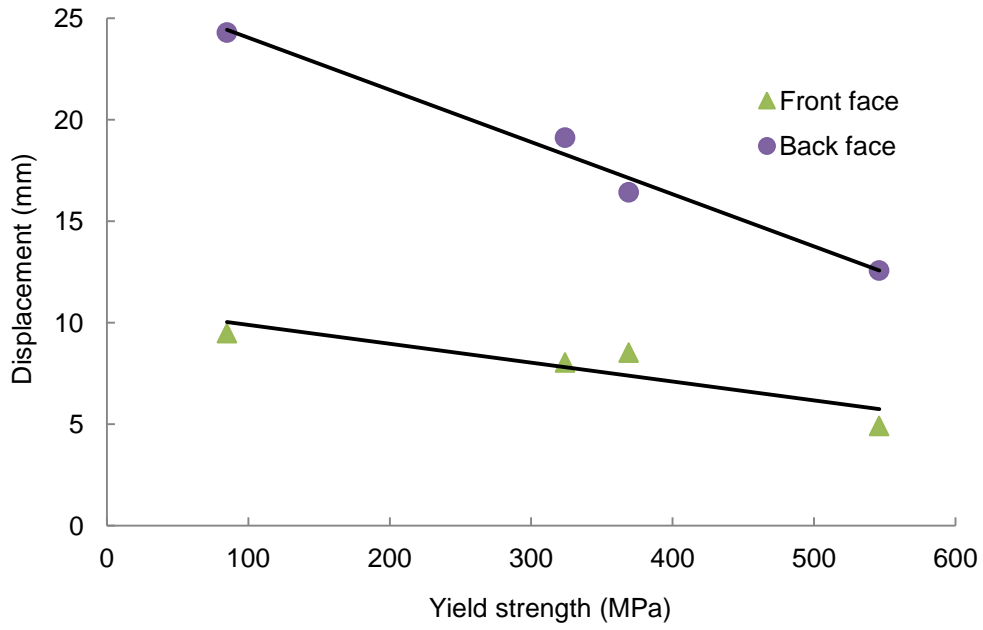


Figure 6: Residual front and back face displacements of the A4T32-4 panel based on the four aluminium alloys versus yield strength.

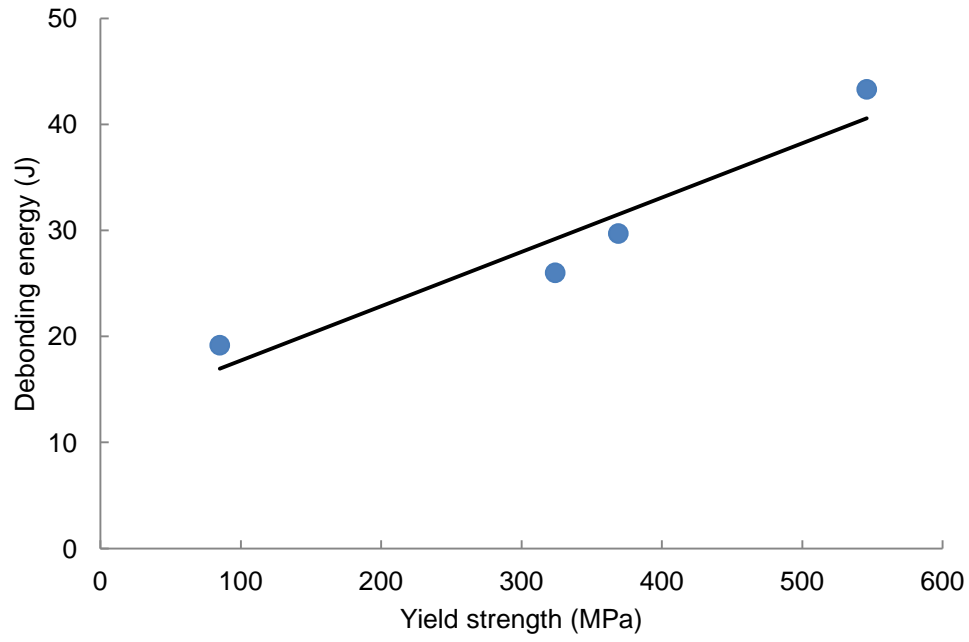
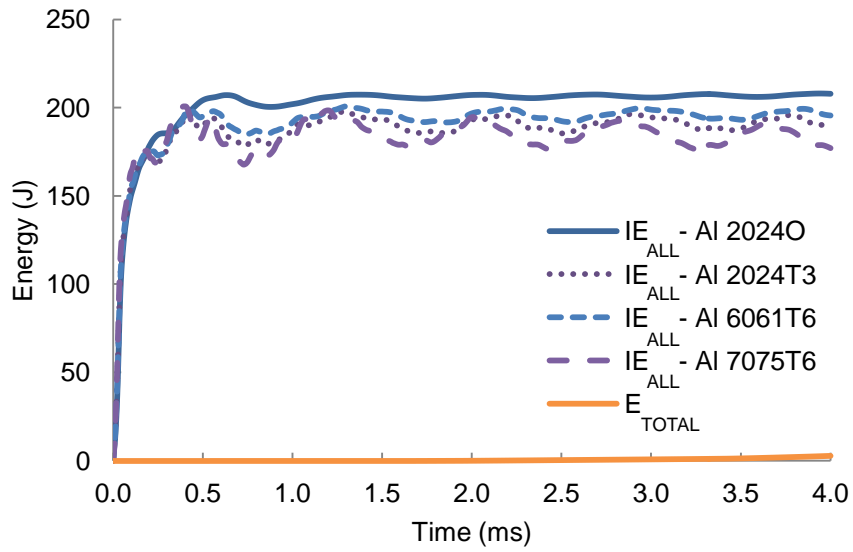
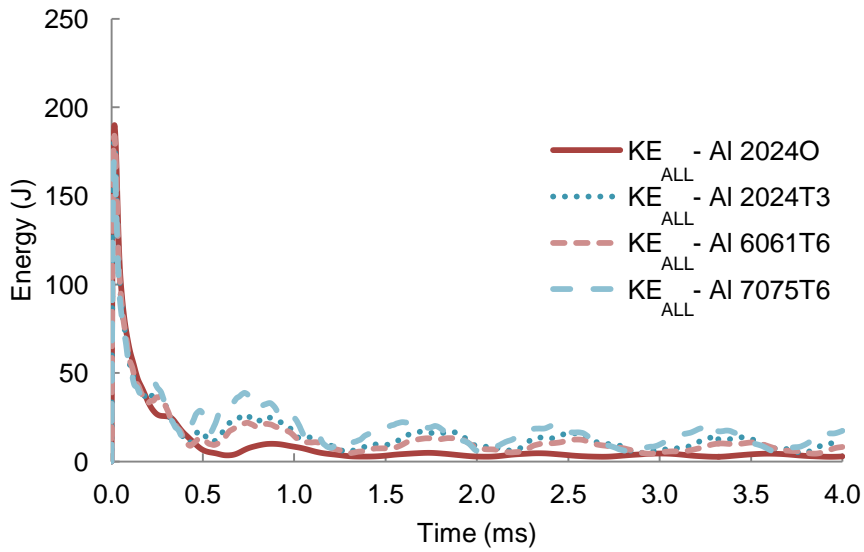


Figure 7: Debonding energy of the A4T32-4 panel based on the four aluminium alloys versus yield strength.



a. Total internal energy ( $IE_{ALL}$ ) and  $E_{TOTAL}$



b. Kinetic energy ( $KE_{ALL}$ ).

Figure 8: The time history of total internal energy and kinetic energy of the A4T32-4 panel based on the four aluminium alloys.

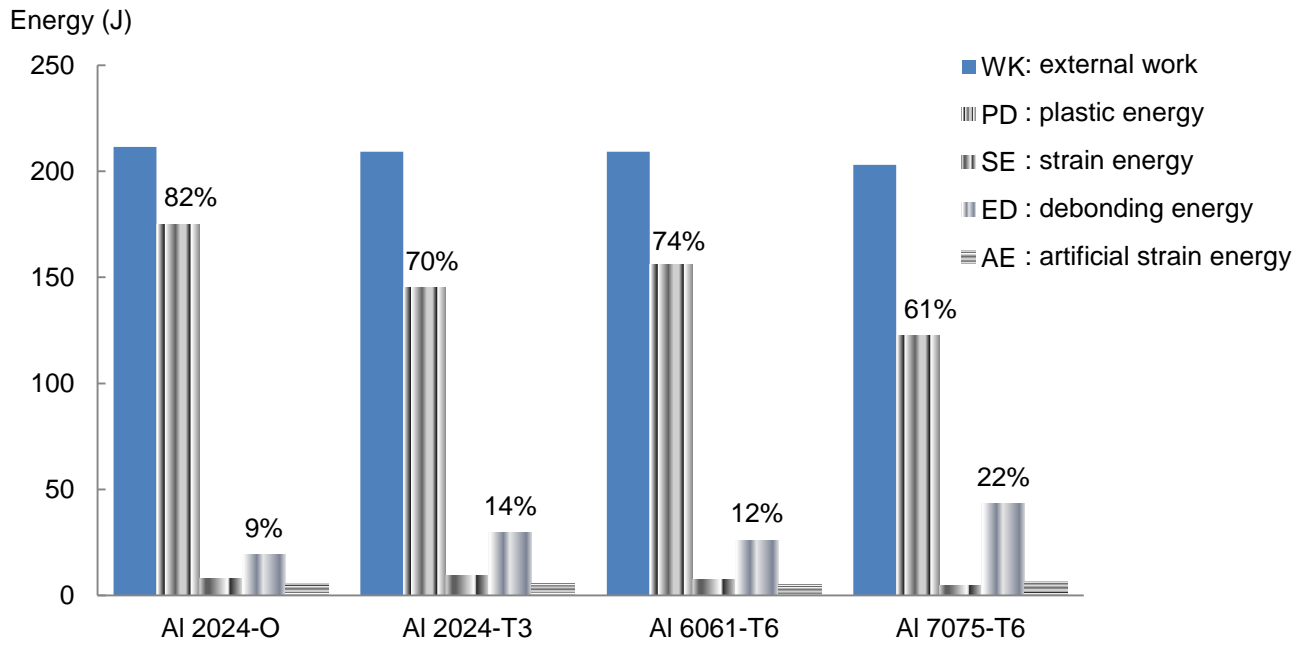


Figure 9: External work and total internal energy components (PD, SE, ED and AE) of the A4T32-4 panel based on the four aluminium alloys.

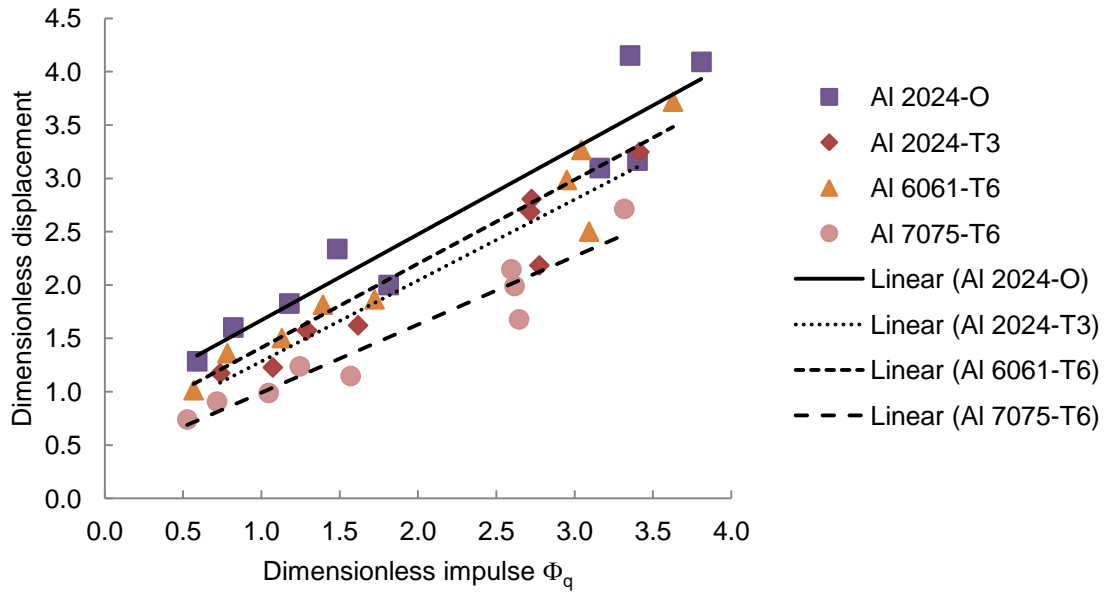


Figure 10: Graph of dimensionless permanent displacement of back face versus dimensionless impulse.



**List of Tables**

Table 1: Details of the lay-ups and impulses for verification.

Table 2: Johnson-Cook constants and static tensile strength for aluminium alloys.

Table 3: Properties of the GFPP layers.

Table 4: Properties of the cohesive layers.

Table 5: Comparison of experimental data from Ref.[9] and numerical simulation results of transient and permanent displacements of front and back faces for verification.

Table 6: Summary of permanent front and back face displacements of FMLs based on the four aluminium alloys.

Table 7: Effective strength values for FMLs of varying composition, based on rule of mixtures approximation.

Table 1: Details of the lay-ups and impulses for verification.

Lay-ups	No. of layers	Thickness (mm)	Impulse (Ns)
A2T18-4	10	5.60	7.94
A3T24-8	11	6.06	7.85
A3T26-3	15	8.10	9.54
A3T28-5	19	9.82	10.34
A4T32-4	10	5.85	7.23
A4T34-5	16	8.73	7.01
A4T36-2	22	11.48	11.61
A4T38-2	28	13.90	11.13
A5T42-4	13	7.46	8.87

Table 2: Johnson-Cook constants and static tensile strength for aluminium alloys.

1  
2  
3  
4  
5  
6  
7  
8  
9  
10  
11  
12  
13  
14  
15  
16  
17  
18  
19  
20  
21  
22  
23  
24  
25  
26  
27  
28  
29  
30  
31  
32  
33  
34  
35  
36  
37  
38  
39  
40  
41  
42  
43  
44  
45  
46  
47  
48  
49  
50  
51  
52  
53  
54  
55  
56  
57  
58  
59  
60  
61  
62  
63  
64  
65

Aluminium type	A (MPa)	B (MPa)	n	C	D <sub>1</sub>	D <sub>2</sub>	D <sub>3</sub>	D <sub>4</sub>	Ultimate tensile strength (MPa)
Al 2024-O [16]	85	325	0.40	0.0083	0.130*	0.130*	-1.500*	0.011*	186
Al 2024-T3 [27]	369	684	0.73	0.0083	0.130	0.130	-1.500	0.011	483
Al 6061-T6 [28]	324	114	0.42	0.0020	-0.770	1.450	-0.470	0.000	310
Al 7075-T6 [29]	546	678	0.71	0.0240	-0.068	0.451	-0.952	0.036	572

\* Damage constants for Al 2024-T3 were used due to the lack of available data.

Table 3: Properties of the GFPP layers.

Elastic properties	Values	Progressive failure	Values
$\rho$ (kg/m <sup>3</sup> )	1800	$X_{1r}$ (MPa)	300
$E_1$ (GPa)	13.0	$X_{1c}$ (MPa)	200
$E_2$ (GPa)	13.0	$X_{2r}$ (MPa)	300
$E_3$ (GPa)	2.40	$X_{2c}$ (MPa)	200
$G_{12}$ (GPa)	1.72	$S_{12}$ (MPa)	140
$G_{13}$ (GPa)	1.72	$S_{13}$ (MPa)	140
$G_{23}$ (GPa)	1.69	$S_{23}$ (MPa)	140
$\nu_{12}$	0.1		
$\nu_{13}$	0.3		
$\nu_{23}$	0.3		

Table 4: Properties of the cohesive layers.

Elastic properties					Damage initiation			Damage evolution		
Thickness	$\rho_c$	$E_n$	$E_s$	$E_t$	$t_n^0$	$t_s^0$	$t_t^0$	$G_n^c$	$G_s^c$	$G_t^c$
$t_c$ (m)	(kg/m <sup>3</sup> )	(GPa)	(GPa)	(GPa)	(MPa)	(MPa)	(MPa)	(J/m <sup>2</sup> )	(J/m <sup>2</sup> )	(J/m <sup>2</sup> )
$10^{-4}$	920	2.05	0.72	0.72	140	300	300	2000	3000	3000

$G_n^c, G_s^c$  and  $G_t^c$  are the critical fracture energies in the normal, the first, and the second shear directions.

$t_n^0, t_s^0$  and  $t_t^0$  are the critical nominal normal stress, the first and the second shear stresses.

Table 5: Comparison of experimental data from Ref. [9] and numerical simulation results of transient and permanent displacements of front and back faces for verification.

Panel	Impulse (Ns)	Numerical				Experiment	
		Transient displ. (mm)		Permanent displ. (mm)		Permanent displ. (mm)	
		Front	Back	Front	Back	Front	Back
A2T18-4	7.94	12.86	28.09	4.95	22.19	9.10	16.30
A3T24-8	7.85	13.06	25.65	6.06	20.34	10.10	19.30
A3T26-3	9.54	12.07	26.91	4.32	20.35	7.20	23.70
A3T28-5	10.34	10.56	28.47	3.23	22.59	2.20	20.90
A4T32-4	7.23	13.91	25.79	9.72	21.73	13.80	17.20
A4T34-5	7.01	10.19	22.19	4.57	17.48	7.60	14.00
A4T36-2	11.61	9.30	32.70	1.55	27.21	5.40	22.60
A4T38-2	11.13	6.82	30.43	1.29	24.59	4.30	20.70
A5T42-4	8.87	13.28	30.32	7.95	25.31	11.50	19.90

Table 6: Summary of permanent front and back face displacements of FMLs based on the four aluminium alloys.

Panel	Aluminium types	Dimensional parameters			Dimensionless parameters		
		Impulse (Ns)	Displacement (mm)		Impulse	Front	Back
			Front	Back			
A2T18-4	Al 2024-O	8.00	5.53	22.92	3.81	0.99	4.09
	Al 2024-T3	8.00	5.17	18.19	3.41	0.92	3.25
	Al 6061-T6	8.00	5.71	20.84	3.63	1.02	3.72
	Al 7075-T6	8.00	4.50	15.20	3.32	0.80	2.71
A3T24-8	Al 2024-O	8.00	6.63	18.77	3.16	1.09	3.10
	Al 2024-T3	8.00	7.10	16.29	2.72	1.17	2.69
	Al 6061-T6	8.00	7.20	18.10	2.95	1.19	2.99
	Al 7075-T6	8.00	5.56	12.07	2.62	0.92	1.99
A3T26-3	Al 2024-O	8.00	4.58	16.21	1.81	0.56	2.00
	Al 2024-T3	8.00	4.42	13.15	1.62	0.55	1.62
	Al 6061-T6	8.00	4.21	15.13	1.72	0.52	1.87
	Al 7075-T6	8.00	2.91	9.30	1.57	0.36	1.15
A3T28-5	Al 2024-O	8.00	3.28	17.99	1.18	0.33	1.83
	Al 2024-T3	8.00	2.41	12.09	1.07	0.24	1.23
	Al 6061-T6	8.00	2.81	14.80	1.13	0.29	1.50
	Al 7075-T6	8.00	1.20	9.74	1.05	0.12	0.99
A4T32-4	Al 2024-O	8.00	9.48	24.29	3.35	1.62	4.15
	Al 2024-T3	8.00	8.52	16.42	2.72	1.46	2.81
	Al 6061-T6	8.00	8.04	19.12	3.04	1.37	3.27
	Al 7075-T6	8.00	4.91	12.57	2.60	0.84	2.15

A4T34-5	AI 2024-O	8.00	4.95	20.42	1.48	0.57	2.34
	AI 2024-T3	8.00	3.02	13.75	1.29	0.35	1.58
	AI 6061-T6	8.00	3.43	15.87	1.39	0.39	1.82
	AI 7075-T6	8.00	1.88	10.82	1.24	0.22	1.24
A4T36-2	AI 2024-O	8.00	2.36	18.41	0.82	0.21	1.60
	AI 2024-T3	8.00	1.21	13.49	0.74	0.11	1.18
	AI 6061-T6	8.00	1.45	15.64	0.78	0.13	1.36
	AI 7075-T6	8.00	0.47	10.44	0.72	0.04	0.91
A4T38-2	AI 2024-O	8.00	1.18	17.88	0.59	0.09	1.29
	AI 2024-T3	8.00	0.68	12.92	0.54	0.05	0.93
	AI 6061-T6	8.00	0.71	14.12	0.57	0.05	1.02
	AI 7075-T6	8.00	0.28	10.30	0.53	0.02	0.74
A5T42-4	AI 2024-O	8.00	7.62	23.63	3.40	1.02	3.17
	AI 2024-T3	8.00	5.26	16.30	2.77	0.71	2.19
	AI 6061-T6	8.00	5.51	18.67	3.09	0.74	2.50
	AI 7075-T6	8.00	2.92	12.53	2.64	0.39	1.68



Table 7: Effective strength values for FMLs of varying composition, based on rule of mixtures approximation.

Lay-ups	Total thickness (mm)	Thickness of aluminium (mm)	Thickness of GFPP (mm)	Aluminium type	Estimated static tensile strength (MPa)
GFPP	N/A	N/A	N/A	N/A	300
A2T18-4	5.60	1.27	4.33	Al 2024-O	274
				Al 2024-T3	342
				Al 6061-T6	302
				Al 7075-T6	362
A3T24-8	6.06	1.91	4.16	Al 2024-O	264
				Al 2024-T3	358
				Al 6061-T6	303
				Al 7075-T6	386
A3T26-3	8.10	1.91	6.20	Al 2024-O	273
				Al 2024-T3	343
				Al 6061-T6	302
				Al 7075-T6	364
A3T28-5	9.82	1.91	7.94	Al 2024-O	278
				Al 2024-T3	335
				Al 6061-T6	302
				Al 7075-T6	353
A4T32-4	5.85	2.54	3.31	Al 2024-O	251
				Al 2024-T3	379
				Al 6061-T6	304

1  
2  
3  
4  
5  
6  
7  
8  
9  
10  
11  
12  
13  
14  
15  
16  
17  
18  
19  
20  
21  
22  
23  
24  
25  
26  
27  
28  
29  
30  
31  
32  
33  
34  
35  
36  
37  
38  
39  
40  
41  
42  
43  
44  
45  
46  
47  
48  
49  
50  
51  
52  
53  
54  
55  
56  
57  
58  
59  
60  
61  
62  
63  
64  
65

---

				AI 7075-T6	418
A4T34-5	8.73	2.54	6.19	AI 2024-O	267
				AI 2024-T3	353
				AI 6061-T6	303
				AI 7075-T6	379
A4T36-2	11.48	2.54	8.94	AI 2024-O	275
				AI 2024-T3	340
				AI 6061-T6	302
				AI 7075-T6	360
A4T38-2	13.90	2.54	11.36	AI 2024-O	279
				AI 2024-T3	333
				AI 6061-T6	302
				AI 7075-T6	350
A5T42-4	7.46	3.18	4.29	AI 2024-O	251
				AI 2024-T3	378
				AI 6061-T6	304
				AI 7075-T6	416